

# SPARC: Spine with Prismatic and Revolute Compliance for Quadruped Robot

Yue Wang<sup>1</sup>

**Abstract**—We present SPARC, a compact, open-source 3-DoF sagittal-plane spine module that combines revolute (pitch) and prismatic (axial) motion with programmable task-space impedance for quadruped robots. The system integrates three torque-controlled actuators, a custom 1 kHz control board, and a protected power unit in a 1.26 kg package, enabling closed-loop stiffness and damping shaping along  $x$ ,  $z$ , and  $\theta$ . We develop an RNEA-based computed-acceleration controller with smooth Stribeck friction compensation to render spring-damper behavior without explicit inertia shaping. Bench experiments validate the approach. Quasi-static push-pull tests show linear force-displacement characteristics with commanded horizontal stiffness spanning 300–700 N/m and  $\leq 1.5\%$  relative error ( $R^2 \geq 0.992$ , narrow 95% CIs). Dynamic displacement-and-release trials confirm mass-spring-damper responses over multiple damping settings, with small, interpretable phase deviations due to configuration-dependent inertia and low-speed friction effects. A task-space PD controller produces roughly linear stiffness but with greater variability and coupling sensitivity. SPARC provides a portable platform for systematic studies of spine compliance in legged locomotion and will be released with complete hardware and firmware resources.

## I. INTRODUCTION

Quadruped mammals use flexible spines to lengthen stride, absorb landing impacts, and generate thrust, achieving agility and efficiency [1] beyond rigid torsos [2]. Most robotic quadrupeds, however, employ rigid trunks to simplify structure and control [3], [4], which constrains energy shaping and workspace modulation at high speed. We target this gap with a compact spine that can bend in the sagittal plane (pitch) and extend axially under active control, providing continuous, tunable compliance.

Prior efforts cover three main directions. Passive spines use elastic elements but are hard to adjust to task demands [5]. Actuated, position-controlled spines behave effectively rigid when holding posture and offer only modest energy benefits [6]. Spring-loaded mechanisms can create axial motion but must be pre-compressed and release open loop, making them single-shot rather than continuously controllable [7]. In contrast, biological spines (e.g., dogs) exhibit loosely coupled vertebrae that allow simultaneous bending and changes in inter-vertebral spacing, i.e., coupled revolute and prismatic motions that support impact attenuation and thrust generation [8]. Compliance is therefore essential for efficient locomotion [9]. What is missing is a compact, replicable spine unit that operates in closed loop, simultaneously realizes revolute and prismatic motions, and provides

\*This work is supported by the School of Electronic and Computer Science (ECS), University of Southampton.

<sup>1</sup>Yue Wang is with the School of ECS, University of Southampton, United Kingdom. Yue.Wang@soton.ac.uk.

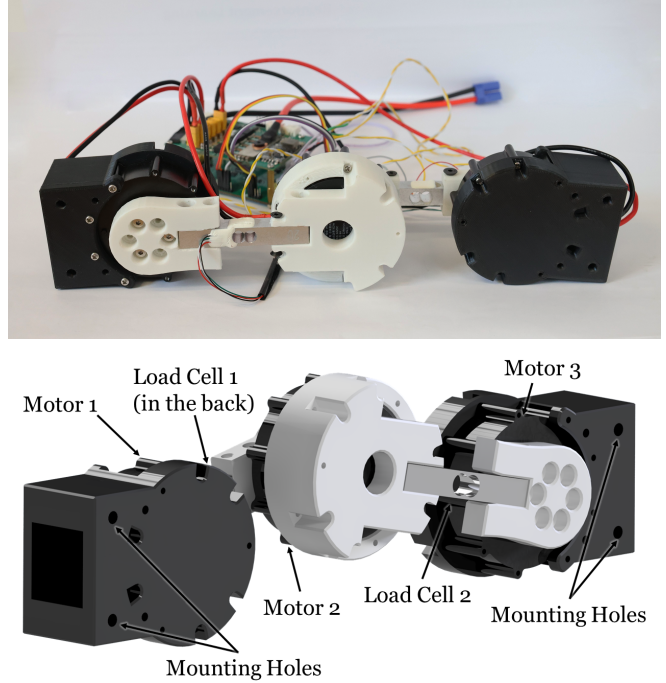


Fig. 1: The compact SPARC system, including a 3-DoF sagittal-plane spine and its control module, is designed to mount between fore and hind body segments. Top: assembled prototype used in experiments. Bottom: structure of the spine unit (bottom).

tunable stiffness and damping for systematic studies on legged platforms.

Motivated by this need, we present **SPARC\*\*** (Spine with Prismatic And Revolute Compliance), a 3-DoF sagittal-plane spine module with torque-controlled actuation and programmable impedance (as shown in Figure 1). SPARC behaves like a software-defined spring-damper along both the linear and rotational axes and mounts between fore and hind body segments to enable controlled, repeatable experiments on spine motion in quadruped locomotion. The contributions of this paper are as follows:

- 1) We present **SPARC**, an open-sourced compact 3-DoF sagittal-plane spine that provides prismatic and revolute motion simultaneously, offering a portable platform to study spine effects in quadruped locomotion.
- 2) We develop an RNEA-based model with Cartesian

\*\*Our design is open-sourced and replication and adaptation are welcomed. Github repository: <https://github.com/YueWang996/xxx>

impedance control and friction compensation to realize tunable linear and torsional stiffness and damping.

- 3) We implement the system and validate it through static and dynamic experiments that quantify the accuracy and repeatability of the commanded stiffness and damping.

The remainder of this paper is organized as follows. Section II reviews spine mechanisms and control approaches and highlights gaps in prismatic motion. Section III details SPARC hardware and control. Section IV presents experiments and analysis. Section V concludes with limitations and future work.

## II. RELATED WORK

Prior work on robotic spines spans revolute-only mechanisms, limited prismatic designs, and multiple pathways to realize compliance. We synthesize these strands and expose what remains missing for *continuous, tunable, axis-selective* spine compliance in legged robots.

*Compliance taxonomy used in this paper:* We distinguish four categories: Passive (P), mechanically variable stiffness (MVS), *joint-level controller-based* (JC), and *task-space (coordinated) controller-based* (TSC). P means the compliance of the spine is generated by elastic materials in the spine. MVS stands for a changeable stiffness of the spine through mechanical structures. JC denotes virtual compliance implemented within individual torque-controlled joints (e.g., QDD drives). TSC denotes system-level compliance that *coordinates multiple joints* to realize *anisotropic* (axis- or mode-selective) stiffness and damping at the module level.

### A. Revolute spinal mechanisms: bending and twisting

Revolute (R) spines have been explored for gait modulation and agility, typically in the sagittal plane (pitch) [6], [11], [12] and for roll-axis twisting [13]. These systems are *R-only* (no axial prismatic DoF) and predominantly use position control or JC at each joint. Reported benefits include torso-leg coordination and turning agility. However, without axial motion, they cannot regulate stride length or absorb landing impacts through controlled extension/compression. Moreover, compliance is often fixed or implicit (structural elasticity) rather than *tunable* in closed loop. Even though when JC is present, it remains per-joint and thus not axis-selective at the module level.

### B. Prismatic or axial motion in spine modules

Real-world spine designs support axial motion is rare. A spring-loaded, precompressed design creates prismatic displacement on demand [7], demonstrating thrust generation but requiring manual preloading and releasing in open loop. As a result, it supports single-shot actions rather than continuous, closed-loop operation. Simulation concepts investigate potential benefits of axial motion [14], but hardware evidence under feedback control remains limited.

### C. Compliance: passive, variable-stiffness, and active

Compliance is central to locomotion efficiency [9] and impact management [15]. Position-controlled spines (e.g., servo-based posture holding) behave effectively rigid during stance and provide only modest energy benefits [6]. Passive elasticity (springs, elastomers) can store and return energy but is difficult to retune across tasks. Variable-stiffness mechanisms adjust mechanical parameters (e.g., spring preload) but operate at limited bandwidth. Quasi-direct-drive (QDD) motors, now common in legged robots, provide high torque transparency. This enables a spine to emulate a mass–spring–damper, with apparent stiffness and damping tuned in real time through impedance control.

### D. Biological perspective and engineering target

In quadrupeds, loosely coupled vertebrae allow simultaneous bending and changes in inter-vertebral spacing, yielding coupled revolute and prismatic motion that supports impact attenuation and thrust generation [8]. This mapping suggests a robotics target: a compact, replicable module that unifies revolute and prismatic DoFs, sustains continuous closed-loop operation, and provides tunable active compliance for systematic evaluation on legged platforms.

## III. METHODOLOGY

This section details the design, modeling, and control of SPARC. We first present the hardware architecture, then describe the dynamic model of the active spine unit and the impedance control law used to achieve compliant, spring-like behavior.

### A. SPARC System Design and Hardware Architecture

The SPARC system is a self-contained unit that integrates three key components: a 3-DoF active spine, a custom Motion Control Board (MCB), and a Power Management Unit (PMU). The overall architecture is shown in Fig. 2, and key hardware specifications for the SPARC system are summarized in Table II.

The active spine is a 3-DoF mechanism designed for motion in the sagittal plane (forward  $x$ , vertical  $z$ , pitch  $\theta$ ), allowing it to produce both prismatic (linear) and revolute (bending) movements. The structure is driven by three QDD BLDC actuators (Xiaomi Cybergear), which provide the high-bandwidth torque control needed for compliant motions. The total mass of the spine unit is 1.26 kg, with lightweight 3D-printed links ensuring that approximately 75% of the mass is concentrated at the actuators. This design reduces the reflected link inertia. For control, torque is primarily estimated using the internal current sensors of the actuators. Additionally, two strain gauge-based load cells are integrated into the central links to provide high-fidelity torque measurements for system validation.

A custom MCB, built around an STM32F405 microcontroller, runs the low-level control loops. The system is designed to achieve a 1 kHz control bandwidth. To meet this timing requirement, the three spine actuators are managed by a single Controller Area Network (CAN) bus channel.

TABLE I: Summary of state-of-the-art spine designs in quadruped robots. Compliance specifies how compliance is realized: Passive (P), mechanically variable stiffness (MVS), joint-level controller-based (JC), task-space (coordinated) controller-based (TSC), or none. JC denotes virtual compliance implemented within individual QDD joints; TSC denotes system-level, anisotropic compliance produced by coordinating multiple joints to realize axis/mode-specific impedance. Adj. (k/b) indicates whether the (virtual) stiffness  $k$  and damping  $b$  are tunable.

Work	DoF (R)	DoF (P)	Actuation	Compliance	Adj. (k/b)	Research Focus
Lynx [10]	✓	✗	Servo + Elastic Material	P	✓/✗	Locomotion study
Bobcat [6]	✓	✗	Servo	None	✗/✗	Efficiency
INU [11]	✓	✗	QDD	JC	✗/✗	Workspace with spine
Yat-sen Lion [12]	✓	✗	QDD	JC	✗/✗	Load leveling (MPC)
Planar Robot [9]	✓	✗	Servo + Spring	VS	✓/✗	Efficiency
Twisting Quadruped [13]	✓	✗	QDD	JC	✗/✗	Agility
SCIQ [7]	✗	✓	Spring	VS	✓/✗	Single-shot thrust
Simulation [14]	✗	✓	N/A	N/A	N/A / N/A	Acceleration/deceleration ability
<b>SPARC (this work)</b>	✓	✓	QDD	<b>TSC</b>	✓/✓	<b>Tunable compliance</b>

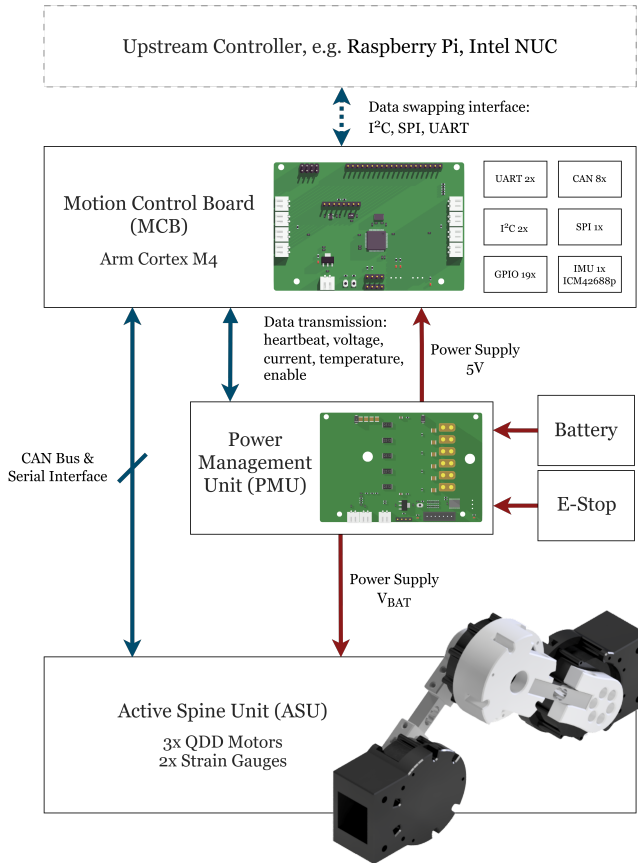


Fig. 2: Hardware architecture of SPARC.

The board also includes an Inertial Measurement Unit (IMU) for attitude estimation and multiple interfaces (SPI, I2C) for communication with an upstream processor.

Power is managed by a custom PMU designed to accommodate the high transient currents of the QDD actuators. The PMU acts as a programmable electronic fuse, employing a hot-swap controller to provide over-current, over-voltage, and thermal protection. An external emergency stop (E-stop) immediately disconnects the DC bus by pulling down the power MOSFET gate. The system accepts either a 6S LiPo

battery or a 24 V bench supply. To withstand burst loads, the PMU uses a 2 mm-thick copper bus and four power MOSFETs rated for up to **192A@100 °C**. The PMU and the Motion Control Board (MCB) communicate over UART and exchange heartbeat signals; if either side fails to receive a heartbeat within a preset window, the PMU's onboard MCU latches a FAULT state and disconnects power.

TABLE II: Key hardware specifications of the SPARC system.

Component	Specification
<b>Active Spine Unit</b>	
Actuator Model	Xiaomi Cybergear (QDD)
Peak Torque per Motor	12 N·m
Gear Ratio	7.75:1
Actuator Mass	317 g
Load Cell Module	20 kg sensor + HX711 ADC
<b>Motion Control Board (MCB)</b>	
Microcontroller	STM32F405RGT6
IMU	TDK ICM-42688-P
CAN Transceiver	SN65HVD232DR
<b>Power Management Unit (PMU)</b>	
Hot-Swap Controller	TI TPS2492PW
Microcontroller	STM32C011F6P6
Power MOSFET	CSD19536KTT

## B. Modeling and Impedance Control

To make the spine behave like a compliant, spring-like mechanism, we developed an impedance controller that relies on a dynamic model to compute motor torques in real time. We model SPARC as a planar open-chain 4-R mechanism operating in the sagittal plane (forward  $x$ , vertical  $z$ , pitch  $\theta$ ). The hardware has three actuated revolute joints, and for seamless integration with a quadruped torso we include a base joint in the model, giving generalized coordinates  $q \in \mathbb{R}^4$ :

$$q = [q_1 \quad q_2 \quad q_3 \quad q_4]^T.$$

In benchtop experiments the base is mechanically fixed so  $\dot{q}_1 = \ddot{q}_1 = 0$  and the associated torque entry is unused,

whereas on-robot  $q_1$  is supplied by the torso state estimator so that the same model applies without changing frames.

With this kinematic convention, the equations of motion are written as

$$M(q)\ddot{q} + C(q, \dot{q})\dot{q} + g(q) = \tau + J^\top(q)F_{\text{ext}}, \quad (1)$$

where  $M(q) \in \mathbb{R}^{4 \times 4}$  is the inertia matrix,  $C(q, \dot{q})\dot{q}$  collects Coriolis and centrifugal effects,  $g(q)$  is gravity, and  $\tau \in \mathbb{R}^4$  are the joint torques. The geometric Jacobian  $J(q) \in \mathbb{R}^{3 \times 4}$  maps joint to task space  $(x, z, \theta)$ , and  $F_{\text{ext}} \in \mathbb{R}^3$  represents an external wrench at the end-effector. Rather than deriving  $M$ ,  $C$ , and  $g$  analytically, we evaluate the Recursive Newton–Euler Algorithm (RNEA) [16] multiple times at the current  $(q, \dot{q})$  with selected  $\ddot{q}$ ; this provides the terms needed by the controller and is computationally feasible on our platform.

The control objective is to render a mass–spring–damper interaction in task space,

$$\Lambda(x)\ddot{\tilde{x}} + D\dot{\tilde{x}} + K\tilde{x} = F_{\text{ext}}, \quad (2)$$

where  $\tilde{x} = x_d - x$ . Yet in this work we adopt a computed-acceleration approach and intentionally neglect explicit  $\Lambda$ -shaping due to the lack of force sensor at the end effector of the spine. Consequently, (2) is used to interpret the rendered interaction rather than to impose a shaped task-space inertia  $\Lambda(x)$ .

Building on this objective, the impedance control law is chosen as

$$\tau_{\text{imp}} = M(q)J^\dagger(q)(\ddot{x}_d - \dot{J}(q, \dot{q})\dot{q}) + J^\top(q)(D\dot{\tilde{x}} + K\tilde{x}) + C(q, \dot{q})\dot{q} + g(q), \quad (3)$$

where a damped least-squares pseudoinverse

$$J^\dagger = J^\top (JJ^\top + \lambda^2 I)^{-1}$$

is used to maintain conditioning near kinematic singularities with a small  $\lambda > 0$ . Because the mechanism is planar, diagonal gains are used,

$$K = \text{diag}(k_x, k_z, k_\theta), \quad D = \text{diag}(d_x, d_z, d_\theta),$$

which correspond to translation along  $x$ , translation along  $z$ , and rotation about the pitch axis  $\theta$ . Note that  $F_{\text{ext}}$  is not measured. Instead, the controller enforces a virtual mass–spring–damper so that any external disturbance manifests as motion  $(\tilde{x}, \dot{\tilde{x}}, \ddot{\tilde{x}})$  satisfying (2).

To further improve tracking on hardware, the commanded torque is augmented with a smooth Stribeck friction model applied at each joint,

$$\tau_{\text{friction}} = \left( \tau_c + (\tau_s - \tau_c) e^{-(|\dot{q}|/|\dot{q}_s|)^a} \right) \tanh(\beta \dot{q}) + b \dot{q}, \quad (4)$$

where  $\tau_c$  and  $\tau_s$  denote Coulomb and static friction,  $b$  is the viscous coefficient,  $\dot{q}_s$  is the Stribeck velocity, and  $a, \beta > 0$  are shape parameters. This smooth approximation avoids chatter near zero velocity while capturing frictional effects at low speed.

### C. Simplified PD Controller

Because the impedance law depends on the model terms  $M$ ,  $C$ , and  $g$ , we also implement a lighter-weight controller that avoids dynamic compensation. The task-space PD form is

$$\tau_{\text{PD}} = J_{\text{task}}^\top(q) (D\dot{\tilde{x}} + K\tilde{x}), \quad (5)$$

where  $J_{\text{task}}(q)$  is the Jacobian from joint to task space  $(x, z, \theta)$  expressed in the base frame, and similarly

$$K = \text{diag}(k_x, k_z, k_\theta), \quad D = \text{diag}(d_x, d_z, d_\theta).$$

This controller is simple and robust, but it does not cancel inertia, Coriolis/centrifugal, or gravity effects. As a result, configuration-dependent steady-state errors and tracking biases can appear, especially under fast motions or large accelerations.

### D. Software and Real-Time Implementation

The control software is written in C and runs on the MCB’s STM32F405 (@168 MHz) under FreeRTOS, which schedules a 1 kHz high-priority control task. Each cycle computes forward kinematics and Jacobians, evaluates inverse dynamics via RNEA (with multiple evaluations as required by the computed-acceleration law), adds the friction compensation, and transmits joint torque commands to the three actuators over CAN. Computationally intensive linear-algebra operations use the Arm CMSIS-DSP library. With these optimizations, a single RNEA pass completes in 17  $\mu\text{s}$  on our platform. When the PD controller is selected, only the task Jacobian is needed; for the planar 4-R open-chain model it admits a closed-form expression and is computed with negligible cost.

## IV. EXPERIMENTS AND ANALYSIS

The design objective of SPARC is to render a task–space spring–damper with tunable coefficients. We therefore evaluate (i) static behavior via quasi–static push–pull tests that characterize  $F_x$  versus horizontal displacement, and (ii) dynamic behavior via displace–and–release trials under multiple damping settings. The benchtop testbed is shown in Fig. 3, and physical parameters are listed in Table III.

TABLE III: Physical parameters of the spine unit

Part	Mass (kg)	Length (mm)	$I_{xx}, I_{yy}, I_{zz}$ ( $\text{kg} \cdot \text{mm}^2$ )
Hind body	0.377	63.2	181, 328, 228
Hind spine	0.376	117.5	148, 502, 426
Front spine	0.414	117.5	991, 175, 990
Front body	0.06	63.2	44, 92, 61

### A. Static Response: Stiffness Rendering

We first test whether the device behaves like a linear spring in the  $x$ –direction. The Cartesian impedance controller is active with diagonal gains  $K = \text{diag}(k_x, k_z, k_\theta)$  and  $D = \text{diag}(d_x, d_z, d_\theta)$ , but desired velocity and acceleration are set to zero. We command five horizontal stiffness values,  $k_x \in \{300, 400, 500, 600, 700\} \text{ N/m}$ , while holding  $k_z = 1000 \text{ N/m}$

TABLE IV: Static stiffness characterization from continuous push–pull tests. OLS = ordinary least squares; CI = 95% analytic confidence interval.

$k_d$ (N/m)	$n$	$\hat{k}$ OLS (N/m)	$R^2$	CI on $\hat{k}$ (N/m)	Rel. err. (%)	Chunk mean $\pm$ SD (N/m)
300	1331	304.315	0.9920	[302.846, 305.785]	1.44	300.646 $\pm$ 11.239
400	1428	401.218	0.9952	[399.776, 402.661]	0.30	395.957 $\pm$ 18.206
500	1795	500.312	0.9964	[498.914, 501.709]	0.06	500.022 $\pm$ 6.909
600	1950	600.252	0.9974	[598.896, 601.607]	0.04	600.877 $\pm$ 7.210
700	1840	697.559	0.9979	[696.097, 699.021]	0.35	699.721 $\pm$ 7.259

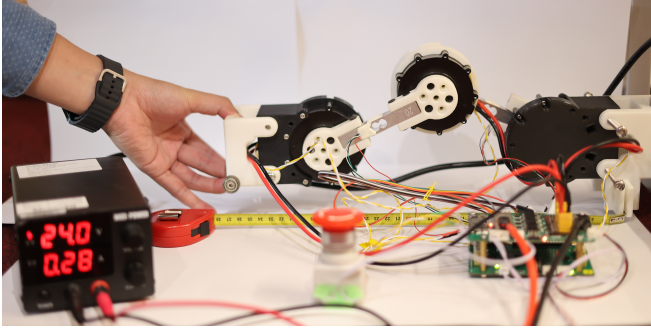


Fig. 3: Testbed of the SPARC system. One end of the spine unit is fixed, and the end effector is floating to avoid friction. A horizontal force  $F_x$  is applied along the  $x$ -axis by pushing/pulling. The ruler is used to indicate the movement of the end effector and the true displacement used for analysis is obtained from encoder-based forward kinematics.

and  $k_\theta = 15 \text{ N} \cdot \text{m}/\text{rad}$  to suppress vertical and rotational motion. The equilibrium is  $x_d = [0.273 \ 0 \ 0]^\top$ . While the control loop estimates torque from motor currents, ground-truth force for analysis is taken from integrated load cells due to current-sensor noise.

For each  $k_x$ , we collect  $> 1,000$  pairs of  $(x, F_x)$  during slow push-pull and fit an OLS line, where Fig. 4 shows force-displacement linearity across the sweep. Table IV reports the estimated stiffness  $\hat{k}_x$ ,  $R^2$ , confidence intervals, and chunk statistics. Measured stiffness closely matches the command with  $\leq 1.5\%$  relative error across the range. The error increases slightly at the lowest stiffness (static friction fractionally larger) and again at the highest stiffness (larger commanded torques increase measurement noise), but the magnitudes remain minor for robotics applications.

### B. Dynamic Response: Damping and Phase Behavior

To further investigate the damping coefficient of the spine, we performed dynamic tests of the SPARC. This test involved displacing the end-effector by a fixed amount ( $0.037 \text{ m}$ ) along the horizontal direction and then releasing it, allowing the system to return to its equilibrium position. We recorded the position of the end effector over time to observe the resulting oscillation. The desired stiffness  $k_d$  was held constant while we tested several different values for the damping coefficient  $b = \{0, 2, 20, 40\} \text{ N} \cdot \text{s}/\text{m}$  for  $k_d = \{300, 500\} \text{ N}/\text{m}$ .

Figure 5 shows the position of the end-effector over time

for several damping coefficients. For each combination of stiffness  $k$  and damping  $b$ , the experiment was repeated 10 times; the shaded areas in the figure represent one standard deviation of these results. At higher damping values (i.e.,  $b = \{20, 40\} \text{ N} \cdot \text{s}/\text{m}$ ), the response of the true system closely matches the ideal mass-spring-damper model. A small, consistent phase difference is still visible, however. This is an expected outcome of the simplified control law, which results in a non-diagonal inertia matrix  $\Lambda(x)$ . This non-diagonal matrix creates coupling effects between the axes of motion [17], which can cause minor phase deviations like those observed.

In the undamped case where  $b = 0$ , the controller attempts to cancel all joint friction using the feedforward compensation from Eq. 4. As the plots show, this leads to a slightly divergent response where the oscillation amplitude grows over time. Accurately identifying the true friction coefficients of a physical system is very difficult, and any error can lead to over-compensation. While a system with a positive-definite damping matrix is guaranteed to be asymptotically stable, this over-compensation likely creates a net negative damping in the system, causing the observed instability.

A different behavior appears at low, non-zero damping (i.e.,  $b = 2 \text{ N} \cdot \text{s}/\text{m}$ ), where the system's response gradually shifts out of phase with the ideal model as the oscillations decay. This occurs because as the oscillation amplitude decreases, the joint velocities also decrease. At these low speeds, the system dynamics become dominated by the complex effects of Stribeck friction. While the main static friction coefficient was identified, other Stribeck parameters—such as the Stribeck velocity ( $\dot{q}_s$ ) and the shape parameter  $\alpha$  are very hard to identify accurately for the real hardware. This slight inaccuracy in the friction model becomes more pronounced at low velocities, causing the phase difference to increase as the system settles.

### C. PD Controller performance evaluation

We finally tested the spine using a simple joint-space PD controller to gauge how much effective task-space stiffness can be produced without full impedance shaping. A handheld luggage scale applies an inline horizontal force  $F_x$  at the end effector while the extension is read against a floor ruler as an indicator of spine movement (Fig. 6). For each proportional gain  $k_p \in \{300, 400, 500, 600\}$  we command a sequence of small, quasi-static displacements in the range shown and record the steady force reading. Each setting is repeated

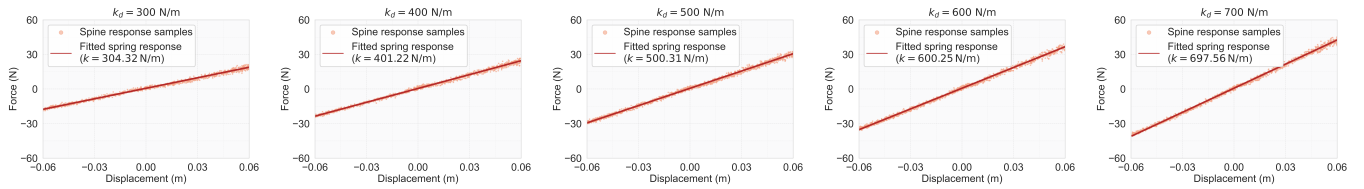


Fig. 4: Static response: measured  $F_x$  vs. displacement for commanded  $k_x \in \{300, 400, 500, 600, 700\}$  N/m. Dots: data; lines: OLS fits whose slopes recover stiffness near the command.

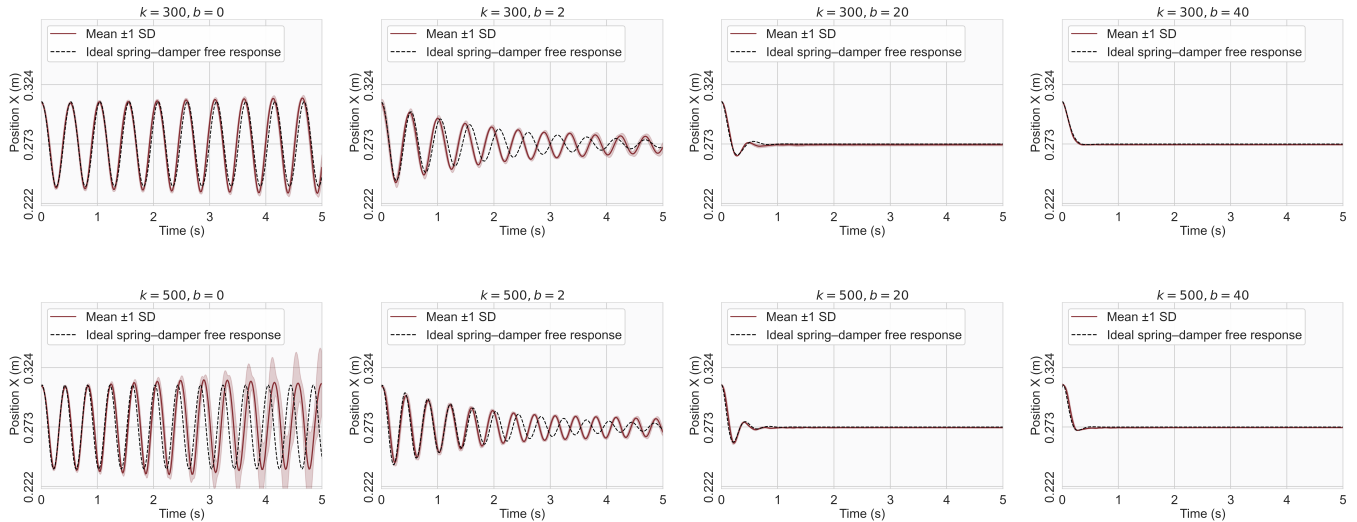


Fig. 5: Dynamic step response of the SPARC system, validating mass–spring–damper behavior. Each panel compares measured hardware response (solid) to the ideal theoretical response (dashed). Top row:  $k = 300$  N/m; bottom row:  $k = 500$  N/m. For each stiffness, four damping coefficients are shown ( $b \in \{0, 2, 20, 40\}$  N·s/m). The solid line is the mean over 10 trials; the shaded region is  $\pm 1\sigma$ .

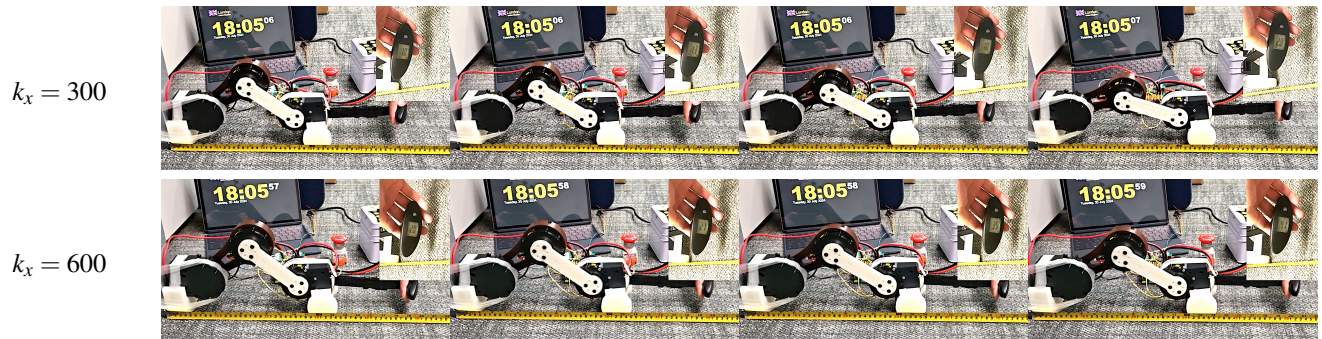


Fig. 6: Spine unit controlled by a PD controller. A handheld luggage scale applies a horizontal force  $F_x$  inline with the spine while extension is read against a ruler on the floor. Rows show  $k_x \in \{300, 600\}$ ; for the same displacement, higher  $k_x$  yields higher measured  $F_x$ , qualitatively indicating greater effective stiffness.

multiple times at each displacement. Fig. 7 demonstrates the mean with  $\pm 1\sigma$  error bars.

Two trends emerge. First, for a fixed displacement, the measured force increases monotonically with  $k_x$  (Fig. 6, row comparison), indicating a higher effective stiffness as proportional action is raised. Second, within each  $k_x$  setting the force–displacement relation is approximately linear over the tested range (Fig. 7), consistent with a spring–like behavior induced by proportional feedback. Compared to the Cartesian

impedance controller, however, the slopes attained by PD control are (i) more sensitive to friction and unmodeled coupling and (ii) exhibit larger trial-to-trial variability at small extensions, as visible in the error bars at low displacement. This is expected because the PD loop does not explicitly regulate task–space axes nor compensate for configuration-dependent inertia, and thus it cannot isolate the  $x$ –direction as effectively as the impedance formulation.

In practice, these results suggest that a PD baseline can

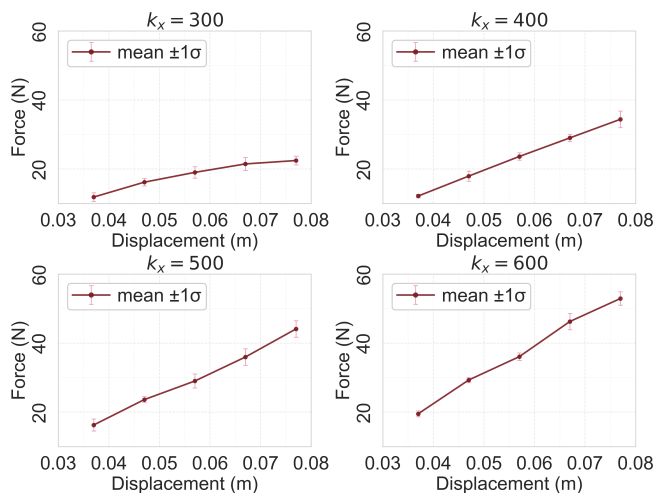


Fig. 7: Displacement–force characteristics of the PD-controlled spine for four proportional gains ( $k_x \in [300, 400, 500, 600]$ ). Each panel shows the mean force with  $\pm 1\sigma$  error bars across repeated trials at each displacement.

provide a tunable and roughly linear stiffness over modest ranges, but precise stiffness targets and repeatability across configurations require the Cartesian impedance controller evaluated in the preceding subsections. The PD characterization therefore serves as a useful lower-complexity benchmark and a sanity check on the mechanical stack, while motivating impedance control when accurate stiffness rendering is desired.

## V. CONCLUSIONS

This work introduced SPARC, a compact 3-DoF sagittal-plane spine module that unifies revolute and prismatic motion under task-space impedance control to deliver tunable, axis-selective compliance. Bench experiments demonstrated accurate stiffness rendering (300–700 N/m with  $\leq 1.5\%$  error) and predictable damping effects, while a task-space PD controller showed greater variability and coupling sensitivity. The main limitation is the absence of on-robot validation. Future efforts will integrate SPARC into a quadruped to investigate the how the stiffness and damping coefficient can affect the robot behaviors.

## REFERENCES

- [1] R. M. Alexander, N. J. Dimery, and R. Ker, “Elastic structures in the back and their role in galloping in some mammals,” *Journal of zoology*, vol. 207, no. 4, pp. 467–482, 1985.
- [2] X. Zhang, C. Zhao, Z. Xu, and S. Huang, “Mechanism analysis of cheetah’s high-speed locomotion based on digital reconstruction,” *Biomimetic Intelligence and Robotics*, vol. 2, no. 1, p. 100033, 2022.
- [3] N. Kau, A. Schultz, N. Ferrante, and P. Slade, “Stanford doggo: An open-source, quasi-direct-drive quadruped,” in *2019 International conference on robotics and automation (ICRA)*. IEEE, 2019, pp. 6309–6315.
- [4] B. Katz, J. Di Carlo, and S. Kim, “Mini cheetah: A platform for pushing the limits of dynamic quadruped control,” in *2019 international conference on robotics and automation (ICRA)*. IEEE, 2019, pp. 6295–6301.

- [5] X. Zhang, H. Yu, B. Liu, and X. Gu, “A bio-inspired quadruped robot with a global compliant spine,” in *2013 IEEE International Conference on Robotics and Biomimetics (ROBIO)*. IEEE, 2013, pp. 1312–1316.
- [6] M. Khoramshahi, A. Spröwitz, A. Tuleu, M. N. Ahmadabadi, and A. J. Ijspeert, “Benefits of an active spine supported bounding locomotion with a small compliant quadruped robot,” in *2013 IEEE international conference on robotics and automation*. IEEE, 2013, pp. 3329–3334.
- [7] K. Ye, K. Chung, and K. Karydis, “A novel lockable spring-loaded prismatic spine to support agile quadrupedal locomotion,” in *2023 IEEE/RSJ International Conference on Intelligent Robots and Systems (IROS)*. IEEE, 2023, pp. 2776–2783.
- [8] B. V. Beaver, *Canine behavior: a guide for veterinarians.*, 1999.
- [9] D. Chen, N. Li, H. Wang, and L. Chen, “Effect of flexible spine motion on energy efficiency in quadruped running,” *Journal of Bionic Engineering*, vol. 14, no. 4, pp. 716–725, 2017.
- [10] P. Eckert, A. Spröwitz, H. Witte, and A. J. Ijspeert, “Comparing the effect of different spine and leg designs for a small bounding quadruped robot,” in *2015 IEEE International Conference on Robotics and Automation (ICRA)*. IEEE, 2015, pp. 3128–3133.
- [11] J. Duperré, B. Kramer, and D. E. Koditschek, “Core actuation promotes self-manipulability on a direct-drive quadrupedal robot,” in *International Symposium on Experimental Robotics*. Springer, 2016, pp. 147–159.
- [12] W. Li, Z. Zhou, and H. Cheng, “Dynamic locomotion of a quadruped robot with active spine via model predictive control,” in *2023 IEEE International Conference on Robotics and Automation (ICRA)*. IEEE, 2023, pp. 1185–1191.
- [13] J. Caporale, Z. Feng, S. Rozen-Levy, A. M. Carter, and D. E. Koditschek, “Twisting spine or rigid torso: Exploring quadrupedal morphology via trajectory optimization,” in *2023 IEEE International Conference on Robotics and Automation*, no. 886, 2023.
- [14] K. Ye and K. Karydis, “Modeling and trajectory optimization for standing long jumping of a quadruped with a preloaded elastic prismatic spine,” in *2021 IEEE/RSJ International Conference on Intelligent Robots and Systems (IROS)*. IEEE, 2021, pp. 902–908.
- [15] G. Chen, M. Ma, S. Guo, H. Lu, and B. Cai, “Mechanism design and performance analysis of bionic quadruped robot with spine,” in *2021 40th Chinese Control Conference (CCC)*. IEEE, 2021, pp. 6685–6690.
- [16] R. Featherstone, *Rigid body dynamics algorithms*. Springer, 2008.
- [17] A. Albu-Schaffer, C. Ott, U. Frese, and G. Hirzinger, “Cartesian impedance control of redundant robots: Recent results with the dlr-light-weight-arms,” in *2003 IEEE International conference on robotics and automation (Cat. No. 03CH37422)*, vol. 3. IEEE, 2003, pp. 3704–3709.